

## Article

# Encapsulation and Delivery of Mitoxantrone Using Zirconium-Based Metal–Organic Frameworks (MOFs) and Their Cytotoxic Potential in Breast Cancer Cells

Mitali Singhal <sup>1</sup>, Kirsten Riches-Suman <sup>2</sup>, Klaus Pors <sup>1</sup>, Matthew A. Addicoat <sup>3</sup>, Amalia Ruiz <sup>1,\*</sup>, Sanjit Nayak <sup>2,4,\*</sup> and Jacobo Elies <sup>1,\*</sup>

- <sup>1</sup> Institute of Cancer Therapeutics, School of Pharmacy and Medical Sciences, Faculty of Life Sciences, University of Bradford, Yorkshire BD7 1DP, UK; mitali3005@gmail.com (M.S.); k.pors1@bradford.ac.uk (K.P.)  
<sup>2</sup> School of Chemistry and Biosciences, University of Bradford, Bradford BD7 1DP, UK; k.riches@bradford.ac.uk  
<sup>3</sup> School of Science and Technology, Nottingham Trent University, Clifton Lane, Nottingham NG11 8NS, UK; matthew.addicoat@ntu.ac.uk  
<sup>4</sup> Bristol Composites Institute, School of Civil, Aerospace and Design Engineering, University of Bristol, Bristol BS8 1TR, UK  
\* Correspondence: g.ruizestrada@bradford.ac.uk (A.R.); s.nayak@bradford.ac.uk (S.N.); j.eliesgomez@bradford.ac.uk (J.E.)

**Abstract:** Mitoxantrone (MTX) is a drug employed in breast cancer treatment, but its application is largely limited due to side effects. A controlled delivery approach can potentially reduce the side effects. In this study, two zirconium (Zr)-based MOFs, UiO-66 and UiO-66-NH<sub>2</sub>, were studied for a more controlled delivery of MTX with a 40% and 21% loading capacity, respectively. Characterisation via powder X-ray diffraction, thermogravimetric analysis, Fourier transform infrared spectrometry, scanning electron microscopy, and dynamic light scattering confirmed the integrity of structure post-MTX loading. UV–vis spectrophotometry revealed distinctive release profiles, with UiO-66-MTX exhibiting a 25% cumulative release after 96 h in water and 120 h in PBS +10% FBS. UiO-66-NH<sub>2</sub>-MTX displayed a more sustained release, reaching 62% in water and 47% in PBS +10% FBS after 168 h. The interaction between MTX and the MOFs was also proposed based on computational modelling, suggesting a stronger interaction of UiO-66NH<sub>2</sub> and MTX, and an optimised interaction of MTX in the tetrahedral and octahedral pores of the MOFs. The study also reports the release profile of the drug and antiproliferative activity against a panel of breast cancer cell lines (MDA-MB-231, MDA-MB-468, and MCF7) and a normal breast epithelial cell line (MCF10A). MTX-encapsulated MOFs were thoroughly characterised, and their biological activity was assessed in vitro. MTT cell viability assay indicated a higher IC<sub>50</sub> value for MTX-loaded MOFs compared to free MTX in physiological conditions, albeit with a slower release profile. These findings suggest the potential of these MTX-loaded MOFs as an alternative avenue for formulation to mitigate side effects.

**Keywords:** metal–organic frameworks; breast cancer; UiO-66; UiO-66-NH<sub>2</sub>; Mitoxantrone



**Citation:** Singhal, M.; Riches-Suman, K.; Pors, K.; Addicoat, M.A.; Ruiz, A.; Nayak, S.; Elies, J. Encapsulation and Delivery of Mitoxantrone Using Zirconium-Based Metal–Organic Frameworks (MOFs) and Their Cytotoxic Potential in Breast Cancer Cells. *Appl. Sci.* **2024**, *14*, 1902. <https://doi.org/10.3390/app14051902>

Academic Editors: Francis Verpoort and Marta Erminia Alberto

Received: 20 December 2023

Revised: 20 February 2024

Accepted: 22 February 2024

Published: 26 February 2024



**Copyright:** © 2024 by the authors. Licensee MDPI, Basel, Switzerland. This article is an open access article distributed under the terms and conditions of the Creative Commons Attribution (CC BY) license (<https://creativecommons.org/licenses/by/4.0/>).

## 1. Introduction

Metal–organic frameworks (MOFs) are coordination networks with an open framework made of organic linkers and inorganic nodes containing potential voids [1–3]. They can interact with drugs in various ways, such as hydrogen bonding, van der Waals forces, aggregation, and encapsulation [4–7]. Unlike conventional drug delivery systems, such as micelles, liposomes, inorganic carriers, and polymers, MOFs have advantages with compositional tunability, which can be useful for engineering interaction with the drugs and their encapsulation [8–12]. By changing either the organic linker or the metal ion or both, MOFs can be tailored for specific drug release properties at the tumour site [13]. Many studies have explored the use of MOFs for cancer treatment, showing their potential in

drug delivery, imaging, and therapy. These studies demonstrate the versatility of MOFs in overcoming the limitations of conventional cancer treatments and provide a basis for further progress in the field of oncology [14,15]. MOFs can be developed using synthetic and natural compounds, employing chemical and physical approaches [16,17]. These MOFs can be endowed with different chemical and physical properties and evaluated for targeted drug delivery in various diseases at the subcellular level [18,19].

Zr-based MOFs are promising materials for biomedical applications such as drug delivery and bio-imaging because of their tunable surface properties, low toxicity, and structural stability in physiological conditions [20]. For instance, Zr-based MOFs have been shown to effectively encapsulate water-soluble azo compounds, exhibiting anticancer effects, especially in the hypoxic conditions of pancreatic cancer [21]. Two separate studies explored the accumulation of the radiotracer  $^{89}\text{Zr}$ -trastuzumab in lesions of metastatic breast cancer patients [22–24] and the use of Zr(IV) ions in the synthesis of nanoscale porphyrin MOFs for the targeted delivery of doxorubicin in liver cancer metastasis in mice [25].

Zr-based MOFs, such as UiO-66 and UiO-66-NH<sub>2</sub> (UiO stands for University of Oslo), are highly stable and can operate at various pH, temperature, aqueous, and physiological conditions [20,26]. UiO-66 (zirconium benzene-1,4-dicarboxylate) is a porous MOF composed of zirconium oxide and hydroxo nodes (ZrO, Zr<sub>6</sub>O<sub>4</sub>(OH)<sub>4</sub>) and benzene-1,4-dicarboxylate (BDC) linkers [26,27]. UiO-66-NH<sub>2</sub> is an analogue of UiO-66 with an amine-functionalised benzenedicarboxylate linker which enables the MOF to interact with drugs or biomolecules by supramolecular interactions, such as hydrogen bonding, for controlled delivery applications [27]. These MOFs exhibit resistance to aqueous and acidic conditions, coupled with robust stability under extreme pressures, reaching up to 10,000 kg cm<sup>-2</sup>, and elevated temperatures, as high as 540 °C [28]. Importantly, both UiO-66 and UiO-66-NH<sub>2</sub> demonstrate hydrolytic stability, which can be attributed to varying pK<sub>a</sub> values originating from the presence of oxo-hydroxy groups within the Zr cluster [29]. UiO-66 and UiO-66-NH<sub>2</sub> have demonstrated successful applications in delivering various anticancer drugs across different cancer cell lines [30–32].

Mitoxantrone (MTX, Figure 1) is a chemotherapeutic agent used to treat different kinds of cancers, especially breast cancer that has spread to other parts of the body [33–37]. However, MTX can also cause serious side effects, such as cardiotoxicity, myelosuppression, and other debilitating side effects. MTX operates by instigating double-strand DNA breaks through the formation of covalent complexes with topoisomerase II, facilitated by its intercalation within the DNA structure [38,39].

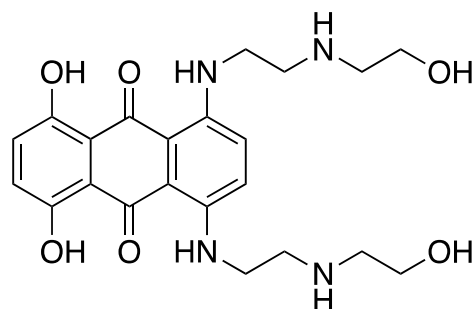


**Figure 1.** Molecular structure of mitoxantrone (MTX) is shown.

One way to improve the effectiveness and delivery of MTX is to use nanocarriers that can carry drugs inside them. These particles can be designed to have specific properties, such as size, shape, and biocompatibility. They can also be used for diagnosis and imaging purposes [40–42]. By using nanocarriers, MTX can be delivered more selectively to the cancer cells, while sparing the healthy cells. This could reduce the dose and frequency of MTX administration and minimise its side effects. Nanotechnology could also help to overcome the resistance that some cancer cells develop to MTX over time. Drug delivery

is an important aspect of cancer therapy, as it can enhance the drug's concentration and activity in the tumour tissue [43].

MOFs have caught much attention recently for potential drug delivery applications [37,40,41,44]. The main objective of this study was to explore the physicochemical aspects, especially the surface properties of UiO-66 and UiO-66-NH<sub>2</sub>, as carriers for MTX, with the idea of revealing how the surface characteristics of the MOFs influence drug interactions. MTX loading and drug release profiles were investigated under biologically relevant conditions, elucidating their impact on breast cancer and normal cell toxicity.

The results of this study demonstrate that UiO-66-NH<sub>2</sub> (despite presenting a lower loading capacity than UiO-66) presents a slower and more consistent MTX release for prolong duration (maintaining an effective concentration). The slow-release nature of UiO-66-NH<sub>2</sub> might contribute towards reduced cytotoxicity. All this suggests that the presence of amino groups may be responsible to enhance controlled drug release and has the potential to address key challenges related to MTX administration in cancer therapy. Further computational modelling was also conducted, which predicts the interaction between MTX and the MOFs and supports the trend in loading capacity and the slow release observed for UiO-66-NH<sub>2</sub>.

## 2. Materials and Methods

### 2.1. Materials

All solvents were of analytical grade and sourced from Fischer Scientific (Loughborough, UK), and the reagents and chemicals were purchased from Sigma-Aldrich (Birmingham, UK). No further purification of the chemicals was carried out.

Cell culture reagents: Roswell Park Memorial Institute (RPMI) 1640 media, L-glutamine (200 mM–G7513), foetal bovine serum (FBS), and dimethyl sulfoxide (DMSO), were purchased from Sigma-Aldrich. Trypsin-EDTA 0.5% was obtained from Gibco (Milton, UK), and phosphate-buffered saline (PBS) was acquired from Severn Biotech (Kidderminster, UK). MTT Formazan was sourced from Merck, Sigma (Birmingham, UK). Tissue culture flasks (25 cm<sup>2</sup> and 75 cm<sup>2</sup>) and 96-well plates (flat- and round-bottomed) were obtained from Sarstedt (Leicester, UK). The cell lines utilised in this project were MDA-MB-231, MDA-MB-468, and MCF-7, all of which were obtained from the American Type Culture Collection (Manassas, VA, USA).

### 2.2. Experimental

#### 2.2.1. UiO-66 Synthesis

UiO-66 was synthesised according to the reported method by Taddei et al. [45]. Zirconium tetrachloride (0.35 g, 1.5 mmol) was added to a 40 mL Teflon vial, followed by addition of 15 mL of dimethylformamide (DMF), along with 1.3 mL of acetic acid (15 equivalents) and 0.324 mL of water (12 equivalents). The mixture was sonicated for 20 min to ensure the complete dissolution of ZrCl<sub>4</sub>. The resulting solution was then allowed to stand at room temperature for 24 h. Subsequently, 249 mg of 1,4-benzene dicarboxylic acid (BDC) was added to the solution. The BDC was dissolved in 5 mL of DMF, resulting in a 0.3 M stock solution. This addition increased the overall molarity of the mixture to 0.1 M. The entire mixture was sealed in a Teflon-lined glass vial and placed in an oven at 120 °C for 24 h, with a heating rate of 5 °C min<sup>-1</sup>, and cooling to 25 °C, at a cooling rate of 2 °C min<sup>-1</sup>. The resulting mixture was centrifuged at 3500 rpm for 20 min, and the resulting solid was washed and soaked in 20 mL of DMF for an additional 24 h. Following this, the mixture was centrifuged at the same speed, and the solid was once again washed and soaked, this time in 20 mL of acetone for 24 h. The next day, the obtained UiO-66 material was dried and activated by placing it in a vacuum oven (Jeiotech, OV-12, Busan, Republic of Korea) for 24 h at 70 °C.

### 2.2.2. UiO-66-NH<sub>2</sub> Synthesis

ZrCl<sub>4</sub> weighing 630 mg (2.703 mmol) was added to a 40 mL Teflon-lined sample vial. To this, 15 mL of DMF and 1 mL of hydrochloric acid (HCl) were added. The mixture was then sonicated in a water bath at 25 °C for 20 min, ensuring complete dissolution of ZrCl<sub>4</sub>. Next, 2-amino terephthalic acid (BDC-NH<sub>2</sub>) weighing 0.898 g (5.408 mmol) was added to the Teflon vial, along with an additional 10 mL of DMF. The reaction mixture was sealed and placed in an oven at 80 °C for 24 h [46]. After the completion of the reaction, the solid precipitates were collected by centrifugation and washed with DMF and methanol. Solvent exchange was performed by immersing MOFs in methanol for 30 min. The solvents were then decanted, and the resulting solid was dried at 115 °C for 24 h under vacuum using a vacuum oven. This drying process ensured the removal of any residual solvents and moisture from the synthesised UiO-66-NH<sub>2</sub> compound (Figure S1).

### 2.3. MTX Loading in MOFs

To determine the optimal conditions, several experiments were conducted by varying the drug concentration and contact time. The best conditions were identified through these experiments. In optimal loading conditions, 3 mg of MOFs was suspended in different proportions with 1 mL of a 3 mg/mL MTX solution in water. The mixture was then probe-sonicated for 30 s. Subsequently, the mixture was placed in a water bath sonicator for 90 min at 25 °C. Following this, the mixture was transferred to a rotor shaker and incubated for an additional 22.5 h. After the incubation period, centrifugation was performed at 13,000 rpm for 5 min in a dialysis ultrafiltration Eppendorf (2 mL), and the filtrate was collected to calculate the amount of loaded drug. The loaded MOFs were then washed with water 7–8 times, collecting the filtrate until the blue colour of MTX disappeared in the filtrate (Figures S2 and S3). A working concentration that provided an absorbance of approximately 1, with a path length of 1 cm, was used to obtain accurate results before and after loading using an UV-vis spectrometer (Perkin Elmer) (Tables S1–S5). To evaluate the loading capacity of MTX, the following Equation (1) was used:

$$\text{Loading capacity (\%)} = \frac{\text{mass entrapped drug}}{\text{mass nanoparticle}} * 100 \quad (1)$$

### 2.4. Characterisation

#### 2.4.1. UV-Visible Absorption Behaviour

The immobilisation of MTX on MOFs was confirmed by UV-vis spectroscopy. The UV-vis absorption behaviour of a solution containing 50 µM of MTX, UiO-66, UiO-66-MTX, UiO-66-NH<sub>2</sub>, and UiO-66-NH<sub>2</sub>-MTX in water was investigated. The UV-vis spectrum of MTX exhibited strong absorbance near 608 and 660 nm (Figure 2), corresponding to the dimer and monomer of the drug, respectively [47]. The absorbance at 608 nm was produced due to electron shift of substituent hydroxy group, and 660 nm was due to the substituent amino group attached to the anthraquinone ring [48]. UiO-66-NH<sub>2</sub> and UiO-66 showed no absorbance at wavelength range from 400 to 800 nm [49]. Due to electrostatic interaction between the cationic MTX molecules and MOFs, absorbance was expected to decrease in host-guest inclusion complex of UiO-66-MTX and UiO-66-NH<sub>2</sub>-MTX compared to free MTX as depicted in Figure 2A,B.

A calibration curve (Figure S4) was constructed at 608 nm for MTX using UV-vis absorption of MTX solutions at different concentrations, ranging from 0.5 µM to 100 µM, in water. This curve served as a reference to determine the loading concentrations of MTX in the MOFs and the release concentrations of MTX from the MOFs.

#### 2.4.2. Thermogravimetric Analysis (TGA)

Approximately 5 mg of each MOF sample was loaded into a platinum pan for analysis using a TGA Instruments Q5000IR thermogravimetric analyser (New Castle, DE, USA). The temperature of the samples was gradually increased from 30 °C to 600 °C at a heating

rate of  $5\text{ }^{\circ}\text{C min}^{-1}$ , under a nitrogen purge gas flow of  $25\text{ mL/min}$ . The obtained data were analysed using Universal Analysis 2000 by TA Instruments (New Castle, DE, USA) software, allowing for the interpretation and evaluation of the thermal properties and decomposition behaviour of the MOF samples.

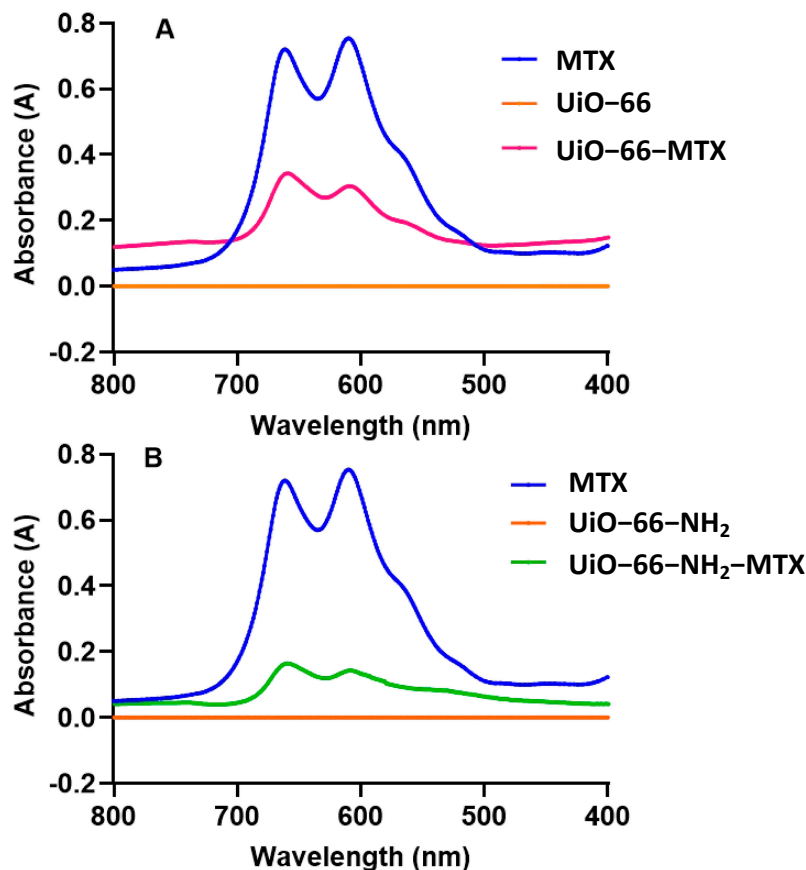


**Figure 2.** UV-vis absorption spectrum for  $50\text{ }\mu\text{M}$  solution in water for (A) MTX, UiO-66, and UiO-66-MTX and (B) MTX, UiO-66-NH<sub>2</sub>, and UiO-66-NH<sub>2</sub>-MTX.

#### 2.4.3. Powdered X-ray Diffraction (PXRD)

MOFs were analysed using PXRD. The PXRD measurements were performed using a Bruker AXS X-ray powder D8 diffractometer (Karlsruhe, Germany). The samples were scanned at  $45\text{ kV}$  and  $40\text{ mA}$ , utilising Cu K $\alpha$  radiation ( $\lambda = 1.54\text{ \AA}$ ,  $1600\text{ W}$ ). A step size of  $0.033$  (corresponding to  $10.08\text{ s}$  per step) was employed, covering the  $2\theta$  range of  $5\text{--}60^{\circ}$ . To minimise background scattering, zero-background discs were utilised during the measurements. The PXRD diffraction patterns obtained were subsequently processed using DIFFRAC.EVA software package (2011) from Bruker (Karlsruhe, Germany), enabling the analysis and interpretation of the crystallographic information and structural characteristics of the MOF samples.

#### 2.4.4. Dynamic Light Scattering (DLS)

DLS was employed to analyse the colloidal properties of the samples before and after functionalisation. The measurements were conducted using a Malvern Nano Zetasizer (UK) instrument. Pure water was used as the dispersion medium during the analysis, and the measurements were performed at room temperature. For the particle size measurements, a plastic cuvette was utilised, while the charge measurements of the samples were carried out using a capillary cell Zetasizer cuvette. Solutions of  $1\text{ mg/mL}$  of both loaded and unloaded MOFs were prepared in water, and measurements were conducted in triplicate.

#### 2.4.5. Fourier Transform Infrared (FTIR) Spectrometry

The functional group modifications of the MOFs, both before and after chemical exposure, were analysed using a Perkin Elmer Spectrum 100 FTIR spectrometer (Buckinghamshire, UK). The FTIR instrument was equipped with universal Attenuated Total Reflectance sampling accessories. For each sample, sixteen scans were performed and then averaged to obtain reliable results. The spectral range covered was from  $4000\text{ cm}^{-1}$  to  $650\text{ cm}^{-1}$ , with a resolution of  $4\text{ cm}^{-1}$ . This FTIR analysis allowed for the identification and characterisation of the functional groups present in the MOFs and provided insights into any changes that occurred after the drug loading.

#### 2.4.6. Scanning Electron Microscopy (SEM) of Crystals

The surface morphology of the synthesised samples was examined using a field emission FEI Quanta 400 E-SEM instrument (West Chester, PA, USA). High-resolution images were captured at 20 KV to provide detailed information about the samples' surface. Prior to the measurement, the samples were mounted on a carbon tape and coated with gold using the Emitech K550 coating system.

#### 2.5. Drug Release Studies

Test tube release studies were conducted to assess the release profile of the MOFs. A total of 10 mg of dried MOFs was added to 5 mL of water, and another set was prepared using PBS supplemented with 10% FBS. The samples were placed in an incubator on a shaker with a speed of 200 rpm at  $37\text{ }^{\circ}\text{C}$ . At specific time points (24 h, 48 h, 72 h, 96 h, 120 h, 144 h, and 168 h), a volume of 1 mL of the release medium was collected using a syringe equipped with a  $0.22\text{ }\mu\text{m}$  PES filter. After each collection, an equal volume of fresh solvent (1 mL) was added to maintain a constant volume throughout the release study. The absorption of release medium was measured using UV-vis spectrophotometer (Figure S5).

#### 2.6. Cell Culture

MDA-MB-231, MCF7, MDA-MB-468, and MCF10A cells were obtained from ATCC (Figure S6). The cells were cultured in RPMI 1640 (Gibco) medium containing 10% FBS, 1% L-Glutamine, 1% sodium pyruvate, and antibiotics (100  $\mu\text{g}/\text{mL}$  streptomycin) for 2–3 days at  $37\text{ }^{\circ}\text{C}$  under a humid atmosphere with 5%  $\text{CO}_2$ . Before passaged, they were harvested by trypsin and resuspended in fresh medium.

#### 2.7. Cytotoxicity Study

The cytotoxic effects of MTX, UiO-66, UiO-66-MTX, UiO-66-NH<sub>2</sub>, and UiO-66-NH<sub>2</sub>-MTX were assessed on MDA-MB-231, MDA-MB-468, and MCF-7 cell lines using the MTT assay. Cells were cultured in 96-well plates at a seeding density of 2000 cells per well and incubated overnight at  $37\text{ }^{\circ}\text{C}$  with 5%  $\text{CO}_2$ . Next day, the cells were subjected to different concentrations of UiO-66-MTX (UiO-66 and MTX loaded at a 1:1 ratio), UiO-66-NH<sub>2</sub>-MTX (UiO-66-NH<sub>2</sub> and MTX loaded at a 1:0.25 ratio), and free MTX at corresponding concentrations (0, 0.1, 1, 10, 100, 1000, and 5000 nM) for 96 h. After the respective incubation periods, the culture medium was removed, and each well received 0.5 mg/mL of MTT solution in fresh medium. This solution was incubated for an additional 4 h at  $37\text{ }^{\circ}\text{C}$ . Following this incubation, the medium was aspirated, and 150  $\mu\text{L}$  of DMSO solvent was added to each well, subjected to pipetting 10–15 times to ensure complete solubilisation of formazan crystals. The absorbance was then measured at a wavelength of 540 nm using a Flexi Station 3 Multi-Mode Microplate Reader. The results are expressed as percentages of cell viability, and all experiments were conducted in 3 independent replicas, with the results being reported as averages.

#### 2.8. Statistical Analysis

The statistical analysis of the data was conducted using two-way analysis of variance multivariate comparison utilizing GraphPad software (Prism 9). For each experimental

assay, triplicate measurements were performed in parallel. The results are presented as the mean value  $\pm$  standard error mean (SEM). In this analysis, significance was determined for  $p$ -values less than 0.05.

### 3. Results and Discussion

#### 3.1. MTX Loading

Various ratios of MOFs and MTX were tested to determine the optimal loading conditions for UiO-66 and UiO-66-NH<sub>2</sub> (Table 1).

**Table 1.** MOF loading capacity (LC%). Values reported are the average  $\pm$  SD of 3 independent repeats of the experiment.

Weight Ratio MOF:MTX [mg:mg]	UiO-66-LC%	UiO-66-NH <sub>2</sub> -LC%
1:1	40.7 $\pm$ 1.4	8 $\pm$ 1.3
2:1	29.6 $\pm$ 1.0	8 $\pm$ 1.7
4:1	15.8 $\pm$ 0.3	21.41 $\pm$ 0.1

Three different concentrations of MTX (3 mg/mL, 1.5 mg/mL, and 0.750 mg/mL) were tested with constant concentration of UiO-66 (3 mg/mL) and UiO-66-NH<sub>2</sub> (3 mg/mL). The results of LC% in Table 1 are presented for three independent loading experiments out of >20 independent repeats.

UV-vis spectrometry was used to confirm the loading of MTX by measuring the absorbance of the supernatant collected after loading UiO-66 and UiO-66-NH<sub>2</sub> [48,50]. A visual change in coloration of the MOFs after MTX incorporation, changing from white to blue for complexed UiO-66-MTX and UiO-66-NH<sub>2</sub>-MTX, was observed. The maximum LC (~40%) (Table 1) was achieved with a weight ratio of UiO-66:MTX of 1:1, corresponding to the adsorption of 0.371 mg of MTX onto 1 mg of UiO-66. The LC% decreased to ~30% with a 2:1 weight ratio and ~15% with a 4:1 weight ratio. In contrast, the UiO-66-NH<sub>2</sub> results demonstrated a reverse trend as compared to UiO-66 in terms of loading MTX. UiO-66-NH<sub>2</sub> showed a maximum loading capacity of ~21% with a 4:1 UiO-66-NH<sub>2</sub>:MTX weight ratio, corresponding to the adsorption of 0.208 mg of MTX loaded per mg of UiO-66-NH<sub>2</sub>. Increasing the weight ratio to 2:1 and 1:1 resulted in a decreased LC of ~8% under the same loading conditions. The greater loading capacity of UiO-66 at higher MTX weight ratios can be attributed to its larger surface area and pore size, whereas the surface area and pore size of UiO-66-NH<sub>2</sub> decreased due to the presence of functionalised groups. The surface area and pore volume of UiO-66 have been reported to be ( $S_{\text{BET}}$ ) 838 m<sup>2</sup>/g and 0.245 cm<sup>3</sup>/g, respectively, compared to UiO-66-NH<sub>2</sub>, which has a surface area ( $S_{\text{BET}}$ ) and pore volume of 822 m<sup>2</sup>/g and 0.236 cm<sup>3</sup>/g, respectively, as reported by Cao et al. [46]. Another report of UiO-66 and UiO-66-NH<sub>2</sub> showed a surface area ( $S_{\text{BET}}$ ) of 857 m<sup>2</sup>/g and 826 m<sup>2</sup>/g, respectively [51]. The observed decrease in loading capacity of UiO-66-NH<sub>2</sub> with an increasing MTX weight ratio is likely due to the presence of the -NH<sub>2</sub> functional group, which results in a partial blockage of the accessible pore volume for MTX molecules, while MTX attachment to the pore surface may also reduce pore size.

The amine functionalisation in UiO-66-NH<sub>2</sub> alters the surface characteristics, potentially affecting the interactions between the MOFs and MTX. This modification can lead to changes in surface charge, hydrophobicity, or specific binding sites, influencing the adsorption capacity of the drug. Additionally, the amine groups in UiO-66-NH<sub>2</sub> could participate in different types of interactions with MTX compared to UiO-66, affecting the loading behaviour.

#### 3.2. Characterisation

##### 3.2.1. TGA

The decomposition patterns of UiO-66 and UiO-66-NH<sub>2</sub> were determined, with UiO-66 showing a higher decomposition temperature at 480 °C compared to UiO-66-NH<sub>2</sub>,

which exhibited a lower decomposition temperature at 360 °C (Figure 3A,B), as previously reported in the literature [46,52]. Significant weight loss occurred [26,46,53] due to decomposition of the ligands [54]. The weight loss of MTX-loaded MOFs was higher than that of their pristine counterparts, and this is possibly due to a higher proportion of organic compounds in the loaded MOFs leading to their decomposition and lower residual mass. A TGA analysis of UiO-66-NH<sub>2</sub>-MTX showed a similar trend. Quantification of MTX from TGA was not possible due to no sharp change in weight upon decomposition of the drug.

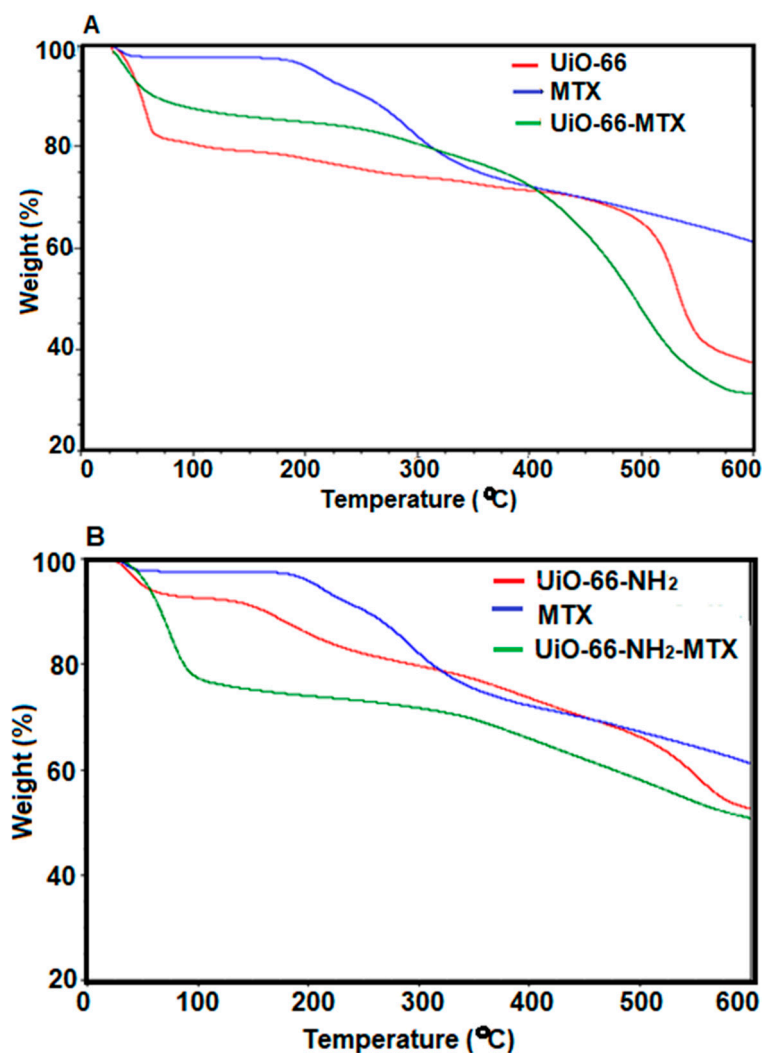


**Figure 3.** TGA plots for (A) MTX, UiO-66, and UiO-66-MTX and (B) MTX, UiO-66-NH<sub>2</sub>, and UiO-66-NH<sub>2</sub>-MTX are shown.

### 3.2.2. PXRD

The powder X-ray diffraction patterns of UiO-66 and UiO-66-NH<sub>2</sub> exhibited similarity with the calculated PXRD patterns for the corresponding MOFs [26,46,51–54] (Figure 4), confirming the phase purity of both MOFs. The PXRD patterns of UiO-66-MTX and UiO-66-NH<sub>2</sub>-MTX are similar to the pristine MOFs, confirming the retention of the crystallinity of the MOFs upon loading of MTX. A slight shift in peak positions and relative intensities in MTX-loaded MOFs suggests a slight change in unit cell due to possible interaction of the drug with the MOFs [55]. Such interactions were further established by computational modelling (see Section 3.5).

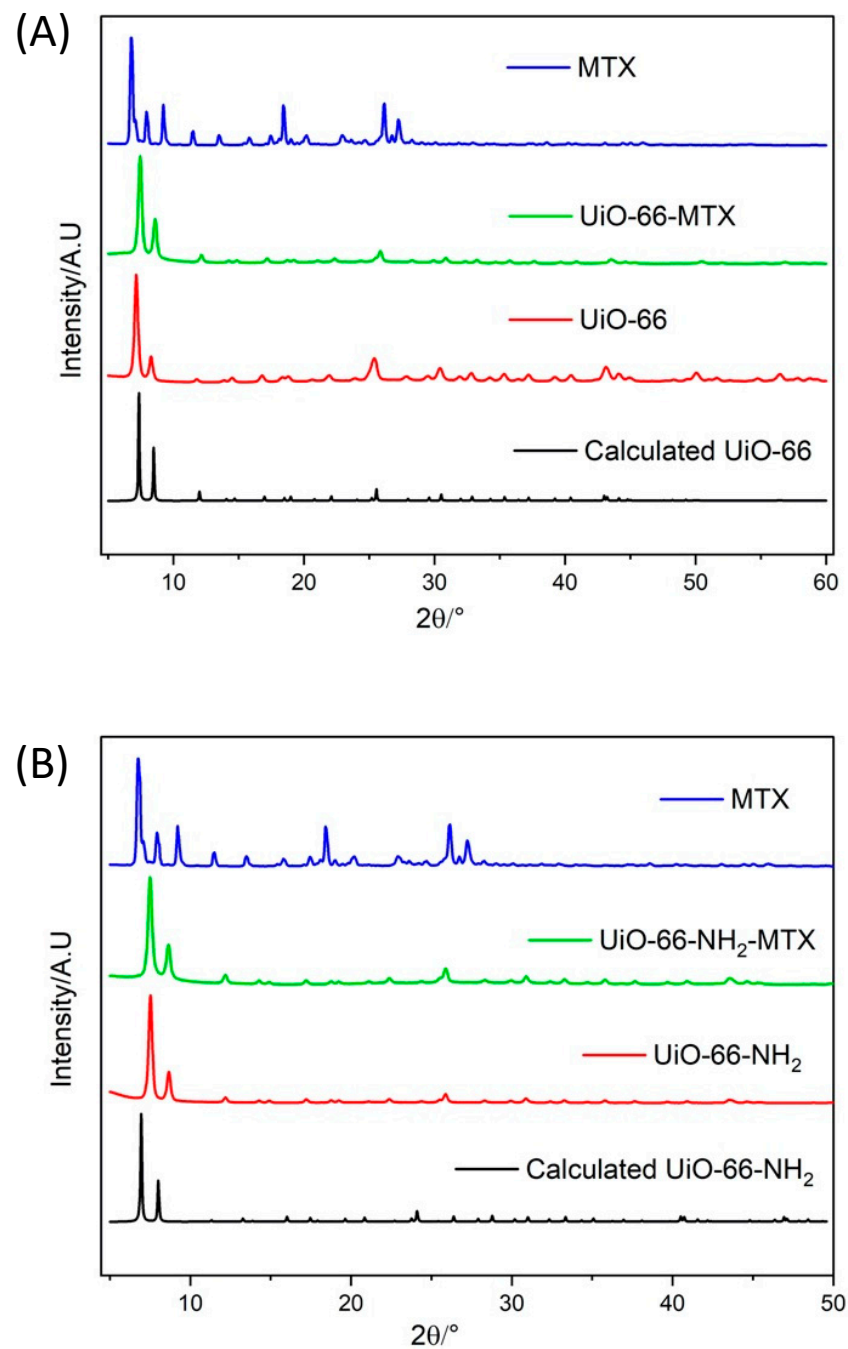


**Figure 4.** PXRD patterns for (A) calculated UiO-66 and pristine UiO-66, UiO-66-MTX, and MTX and (B) calculated UiO-66-NH<sub>2</sub> and pristine UiO-66-NH<sub>2</sub>, UiO-66-NH<sub>2</sub>-MTX, and MTX are shown.

### 3.2.3. DLS

Particle hydrodynamic size, polydispersity, and surface charge were measured before and after loading MTX for UiO-66 and UiO-66-NH<sub>2</sub> in water (Table 2). Synthesis of UiO-66 was performed by an ageing method to obtain nano-sized particles of  $156 \pm 0.4$  nm and a polydispersity index (PdI) of 0.279 for better drug delivery to tumour cells [45]. After MTX loading, the nanoparticles showed an increase in the size of UiO-66-MTX ( $211 \pm 8$  nm) and a PdI of 0.42. UiO-66-NH<sub>2</sub> exhibited a hydrodynamic size of  $170 \pm 2.3$  nm [46] and a PdI of 0.212 before MTX loading and a size of  $487 \pm 3$  nm and a PdI of 0.179 after loading of MTX (Figure S7). The size of UiO-66-NH<sub>2</sub>-MTX was bigger than UiO-66-MTX, and this may be due to the blockage of pores by binding to an -NH<sub>2</sub> group [56].

**Table 2.** Colloidal properties of UiO-66, UiO-66-MTX, UiO-66-NH<sub>2</sub>, and UiO-66-NH<sub>2</sub>-MTX.

MOFs	Size (nm)	PdI	Zeta Potential (mV)
UiO-66	156 ± 0.4	0.279	26.7 ± 2.23
UiO-66-MTX	211 ± 8	0.42	19.8 ± 0.94
UiO-66-NH <sub>2</sub>	170 ± 2.3	0.212	30.8 ± 0.81
UiO-66-NH <sub>2</sub> -MTX	487 ± 3	0.179	14.1 ± 0.66

The surface charge of UiO-66 decreased from  $26.7 \pm 2.23$  mV to  $19.8 \pm 0.94$  mV after loading with MTX, indicating possible internalisation of the drug. MTX contains negatively charged functional groups, which can interact with the positively charged sites on the surface of UiO-66, leading to a decrease in the overall positive charge of the MOFs. This reduction in surface charge might imply that MTX is adsorbed or bound to the MOFs, and the negative charges of MTX contribute to the altered electrostatic characteristics of UiO-66.

The zeta potential of UiO-66-NH<sub>2</sub> decreased from  $30.8 \pm 0.81$  mV to  $14.1 \pm 0.66$  mV after MTX loading, and the particle size of UiO-66-NH<sub>2</sub>-MTX was larger compared to UiO-66-NH<sub>2</sub>. According to Ibrahim et al. (2019), UiO-66 and UiO-66-NH<sub>2</sub> carry a positive charge in aqueous solutions with a pH below 8.3, resulting from the formation of Zr-OH<sup>2+</sup> by Zr-OH at the Zr6 node. Furthermore, at pH levels below 5, UiO-66-NH<sub>2</sub> can undergo protonation at the amino group. These varying surface charges, influenced by factors such as H-bond ability to donate or accept, amino group, Zr cluster, and host-guest chemistry, are utilised to effectively load and deliver MTX [29]. Water stability of UiO-66 and UiO-66-NH<sub>2</sub> at different pH values may be due to different pKa values generated by oxo-hydroxy groups of the Zr cluster [29].

### 3.2.4. FTIR

FTIR spectroscopy was carried out to identify the presence of the functional groups for UiO-66, UiO-66-MTX, UiO-66-NH<sub>2</sub>, and UiO-66-NH<sub>2</sub>-MTX. The FTIR spectra for UiO-66 and UiO-66-NH<sub>2</sub> were found to be similar to reports in the literature [46,51,57]. The symmetrical and asymmetrical stretching of amine generally appears between 3000 and 3400 cm<sup>-1</sup> [51], which was observed in UiO-66-MTX after MTX loading at 3020 cm<sup>-1</sup>, but not in UiO-66. UiO-66 exhibited strong bands at 1585 and 1391 cm<sup>-1</sup>, which indicate the asymmetric and symmetric stretching of O-C-O in the BDC linker. The weak band at 1507 cm<sup>-1</sup> is attributed to C=C stretching of the benzene ring, while the band at 1665 cm<sup>-1</sup> demonstrates the C=O stretching in DMF and its presence in UiO-66 pores. No band at 1685 cm<sup>-1</sup> indicates the absence of any free BDC. The bands at 819, 742, and 663 cm<sup>-1</sup> indicate the bending of -OH and O-C-O and the stretching of C=C and C-H bonds in the BDC linker. The FTIR spectrum of UiO-66-MTX provided evidence for MTX loading, as indicated by similar bands at 1638 and 1608 cm<sup>-1</sup> in place of 1640 and 1607 cm<sup>-1</sup> in MTX. This indicates the C=C stretching of alkene and unsaturated ketones. The slight difference in bands can be attributed to the interaction between MTX and UiO-66. A strong band at 1197 cm<sup>-1</sup> revealed the strong C-O stretching of tertiary alcohol of MTX, which was indicated at 1204 cm<sup>-1</sup>. A weak band at 970 cm<sup>-1</sup> demonstrates the strong C=C bending of the alkene group (Figure 5A).

The FTIR spectrum of UiO-66-NH<sub>2</sub> showed bands at 3352 cm<sup>-1</sup> and 3482 cm<sup>-1</sup>, which were associated with the symmetric and asymmetric vibrations of the -NH<sub>2</sub> groups, respectively [51,57]. A slight shift in these peaks in UiO-66-NH<sub>2</sub>-MTX suggested a bond formation between MTX and UiO-66-NH<sub>2</sub>. The peak at 1648 cm<sup>-1</sup> represented the C=O stretching of DMF and indicated its presence in UiO-66-NH<sub>2</sub> pores. The peak at 1621 cm<sup>-1</sup> in UiO-66-NH<sub>2</sub> showed the stretching vibrations of C-N. Changes in the absorption pattern at 1648 and 1607 cm<sup>-1</sup> in UiO-66-NH<sub>2</sub> indicated the interaction between UiO-66-NH<sub>2</sub> and MTX (Figure 5B).

Strong peaks of UiO-66-NH<sub>2</sub> and UiO-66-NH<sub>2</sub>-MTX at 1482 and 1368 cm<sup>-1</sup> corresponded to the asymmetric (based on DMF presence) and symmetric stretching of O-C-O and C-N in the BDC-NH<sub>2</sub> ligand [51,58]. A weak band at 1431 cm<sup>-1</sup> attributed to the O-H

bending in the carboxylic group, while the bands at 803, 761, and 650  $\text{cm}^{-1}$  indicated a combination of C=C, C-H vibration, O-C-O, and OH bending in the linker. Small changes in these bands in UiO-66-NH<sub>2</sub>-MTX indicated the changes in the chemical environment due to the interaction of MTX and metal ions. The FTIR spectrum of UiO-66-NH<sub>2</sub>-MTX provided evidence for the presence of MTX in the pores of UiO-66-NH<sub>2</sub>. The bands at 1382  $\text{cm}^{-1}$  indicated phenol OH bending of MTX, and 1254  $\text{cm}^{-1}$  demonstrated C-O stretching of the alkyl aryl ether group.

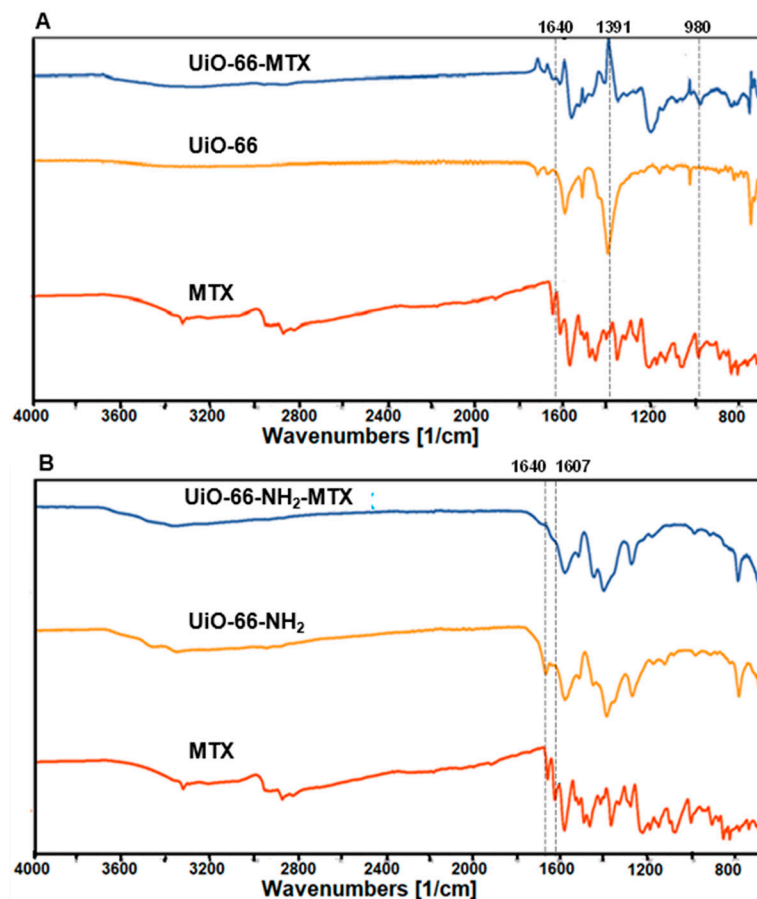


**Figure 5.** FTIR spectra at the wavelength range of 650–4000  $\text{cm}^{-1}$  for (A) MTX, UiO-66, and UiO-66-MTX with the characteristic peaks of MTX found between 980  $\text{cm}^{-1}$ , 1391  $\text{cm}^{-1}$ , and 1640  $\text{cm}^{-1}$  of the UiO-66-MTX spectra and (B) MTX, UiO-66-NH<sub>2</sub>, and UiO-66-NH<sub>2</sub>-MTX with the characteristic peaks of MTX found between 1607  $\text{cm}^{-1}$  and 1640  $\text{cm}^{-1}$  of the UiO-66-NH<sub>2</sub>-MTX spectra.

### 3.2.5. SEM

SEM images revealed the surface morphology of UiO-66, UiO-66-MTX, UiO-66-NH<sub>2</sub>, and UiO-66-NH<sub>2</sub>-MTX as shown in Figure 6. The morphology of UiO-66 and UiO-66-NH<sub>2</sub> is in accordance with the published results [46,54,56]. UiO-66 was synthesised by an ageing process to obtain a nano size, and the difference is obvious in SEM images' appearance (Figure 6A). The size of the UiO-66 crystals is much smaller (also observed from DLS) and tends to form aggregates, compared to UiO-66-NH<sub>2</sub> crystals, which are more well dispersed and uniform. After MTX loading, a slight change was observed for UiO-66-MTX with more diffused agglomeration. However, in the case of UiO-66-NH<sub>2</sub>-MTX, there was no significant change in morphology, and the well-dispersed cubic structure was maintained.

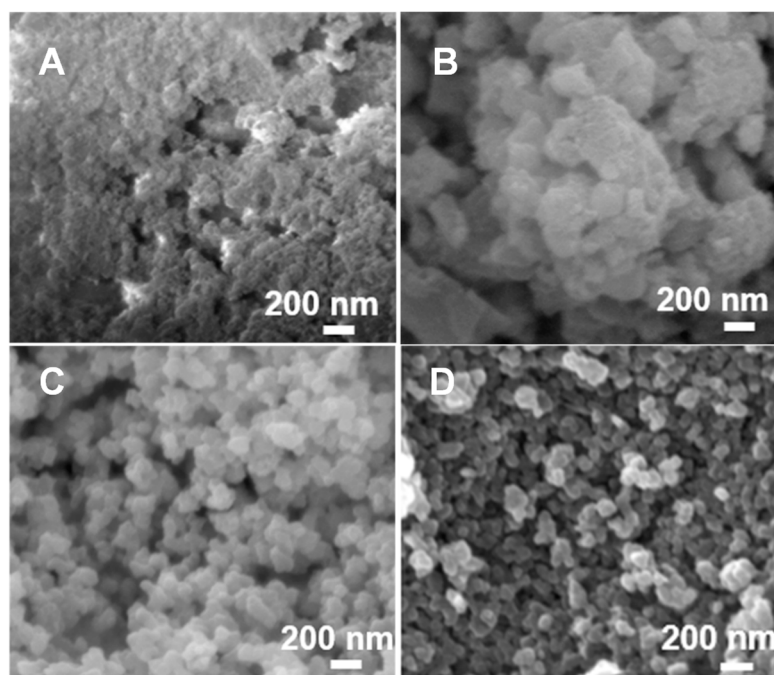


**Figure 6.** SEM images showing surface morphology of (A) UiO-66, (B) UiO-66-MTX, (C) UiO-66-NH<sub>2</sub>, and (D) UiO-66-NH<sub>2</sub>-MTX. The scale bar represents 200 nm. All the images are in same magnification (20 K).

### 3.3. In Vitro Release Studies

The release profile of MTX (Figure 7) from UiO-66-MTX and UiO-66-NH<sub>2</sub>-MTX, in water and in PBS (pH 7.4) +10% FBS at 37 °C, mimicking the culture conditions surrounding cancer cell lines, was investigated. The stability of Zr-based MOFs, particularly UiO-66 and UiO-66-NH<sub>2</sub>, in PBS remains a concern. Previous investigations have indicated potential instability of Zr-MOFs in PBS, prompting the exploration of alternative conditions for drug release studies [1,59–62]. In this study, water and PBS supplemented with 10% FBS was used for drug release experiments. The addition of 10% FBS was deliberate and served a dual purpose: it helped mitigate the observed instability in PBS and introduced biologically relevant components that may influence drug release dynamics. The protein content in FBS-supplemented PBS also simulates the conditions closer to physiological environments, enhancing the clinical relevance of drug release assessments. The results indicate that UiO-66-MTX showed a gradual release of approximately 25% of the drug after 96 h in water at 120 h in PBS +10% FBS, demonstrating the stability of UiO-66-MTX in both water and PBS +10% FBS. UiO-66-NH<sub>2</sub>-MTX showed a slower and more consistent release of MTX with a release of  $62 \pm 4.9\%$  in water and  $47 \pm 3.6\%$  in PBS +10% FBS after 168 h. The percentage release of MTX after 96 h from UiO-66-MTX was lower compared to UiO-66-NH<sub>2</sub>-MTX in water. In PBS +10% FBS, a release of  $20 \pm 2\%$  by UiO-66-MTX and  $19 \pm 4\%$  by UiO-66-NH<sub>2</sub>-MTX was reported, which simulates the culture conditions used for a cytotoxicity assay in different cell lines and agreed with the results obtained after 96 h. The slow release of MTX from both MOFs in PBS at pH 7.4 is consistent with prior findings [63]. The UiO-66-MTX material demonstrated a decrease in release percentage after 96 h in water and after 120 h in PBS +10% FBS. In contrast, the UiO-66-NH<sub>2</sub>-MTX material showed an increase in release percentage until 168 h in both water and PBS +10% FBS. These results demonstrate that, despite UiO-66-NH<sub>2</sub> having a lower loading capacity than UiO-66, it still showed a slow and consistent MTX release for a prolonged duration. The observed slower release profile in the presence of FBS necessitates further discussion to consider its implications on drug delivery. A comparison with the existing literature reveals a common trend where nanoparticles, including liposomes and polymers, often exhibit faster release profiles in biological media due to destabilisation [64–66]. However,

our results with MOFs deviate from this norm. This divergence prompts an exploration of the possible formation of a protein corona around the MOFs, influencing their release kinetics. For instance, the encapsulation of doxorubicin within a BSA-coated ZIF-8 MOF exhibited enhanced biocompatibility, leading to increased uptake by MCF7 breast cancer cells. This phenomenon can be attributed to the positive charge present on the outer surface, facilitating improved interaction with the cellular environment [67]. Importantly, this distinctive behaviour to proteins could present an advantageous feature in MOF-based drug delivery systems [44,68] compared to other nanoparticle formulations.

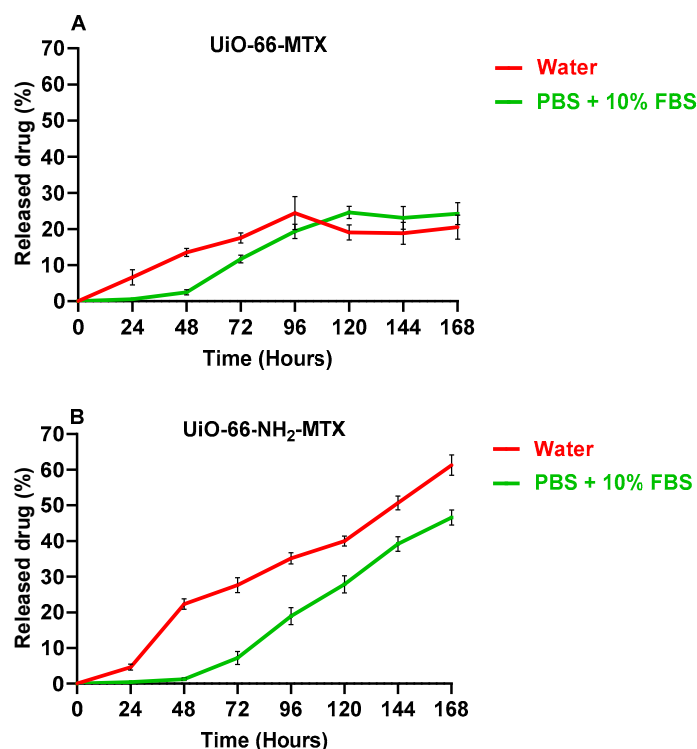


**Figure 7.** Released drug % in water and in PBS (pH 7.4) + 10% FBS at 37 °C over 168 h from (A) UiO-66-MTX and (B) UiO-66-NH<sub>2</sub>-MTX. The data points shown on each figure represent the average  $\pm$  SEM of 3 independent experiments.

### 3.4. Biocompatibility of the Nanocarrier

The cytotoxicity associated with many cancer drugs often gives rise to undesired side effects. To address this concern, nanocarriers that gradually release the drug have emerged as a promising approach for cancer treatment. The primary objective of this study was to compare the toxicity of free MTX with UiO-66-MTX and UiO-66-NH<sub>2</sub>-MTX on monolayer cultures of cancerous cells (MDA-MB-231, MDA-MB-468, and MCF7) and normal breast cell (MCF10A). A series of experiments were conducted to evaluate the impact of different concentrations of all three compounds on cell viability.

#### 3.4.1. Chemosensitivity Assay in Monolayer Culture of Cell Lines with Pristine MOFs

The application of MOFs as drug delivery systems may be constrained by their potential to induce cytotoxicity in normal cells. Prior to utilizing MTX-loaded MOFs, the biosafety of pristine MOFs was evaluated on neoplastic and non-neoplastic cell lines to ascertain their potential toxicity, using the MTT assay (Section 2.7). The cells were subjected to treatment with pristine MOFs under the same culture conditions as the treatment with lower and higher concentrations of UiO-66 and UiO-66-NH<sub>2</sub> in 96-well plates (Figure 8). The cells were incubated with these compounds to evaluate their impact on cell viability. In all tested cell lines, treatments with both UiO-66 and UiO-66-NH<sub>2</sub> consistently maintained cell survival rates above 90%. Importantly, there were no statistically significant differences

in cell viability between the control group and pristine MOFs in any of the examined neoplastic and non-neoplastic cell lines, indicating that the MOFs themselves did not induce cytotoxic effects.

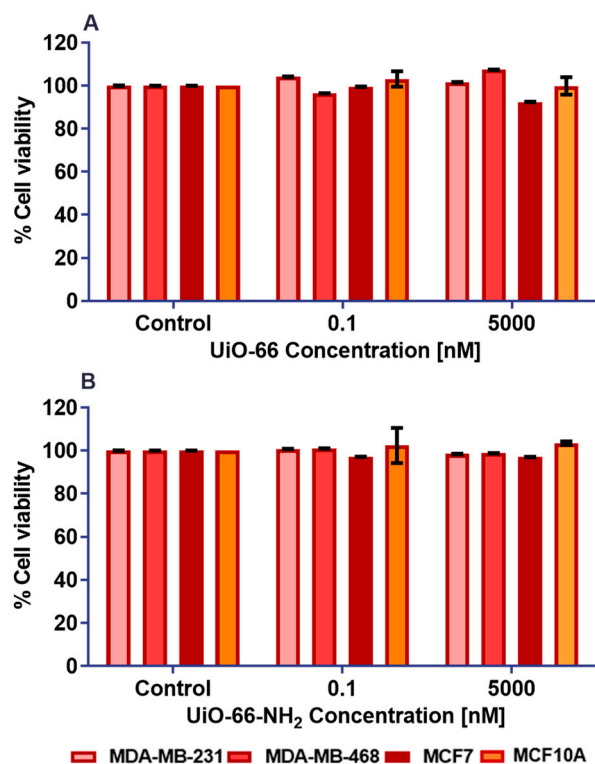


**Figure 8.** Cytotoxicity data obtained in monolayer culture with pristine MOFs. Cytotoxicity profiles of UiO-66 and UiO-66-NH<sub>2</sub> on cell viability after 96 h of treatment. MDA-MB-231, MDA-MB-468, MCF7, and MCF10A cell lines were treated with 0.1 nM and 5  $\mu$ M concentrations of (A) UiO-66 and (B) UiO-66-NH<sub>2</sub>. The data points shown in each figure represent the average  $\pm$  SEM of three independent experiments normalised to the control value for untreated cells.

#### 3.4.2. Cytotoxicity Assay in Monolayer Culture of Cell Lines with Free and Loaded MTX

The anti-proliferative effects of MTX, UiO-66-MTX, and UiO-66-NH<sub>2</sub>-MTX were assessed on all cells with a 10-fold serial dilution of six MTX concentrations (0.1 nM, 1 nM, 10 nM, 100 nM, 1  $\mu$ M, and 5  $\mu$ M) after 96 h of incubation with cancerous and non-cancerous cell lines. The efficacy of MTX-loaded MOFs was evaluated by comparing the IC<sub>50</sub> values obtained in all selected cell lines after treatment (Figure 9).

The IC<sub>50</sub> value (Table 3) against MDA-MB-231 cells for MTX after 96 h of treatment was found to be 29 nM, consistent with prior studies [69,70]. UiO-66-MTX resulted in a decrease in the IC<sub>50</sub> value to 103 nM, while UiO-66-NH<sub>2</sub>-MTX exhibited a decrease to 1  $\mu$ M after 96 h. Similarly, in MDA-MB-468 and MCF7 cells, the IC<sub>50</sub> values of MTX were the lowest, followed by UiO-66-MTX, and they were the highest for UiO-66-NH<sub>2</sub>-MTX. In MCF7 cells, MTX showed IC<sub>50</sub> values of 75 nM, which aligns with the results obtained in a previous study [71]. The incubation of MCF10A cells with MTX-loaded MOFs revealed that UiO-66-NH<sub>2</sub>-MTX exhibited a higher IC<sub>50</sub> value than free MTX, suggesting that the MOF formulations have a lower impact on normal cell proliferation *in vitro*. However, the IC<sub>50</sub> value for UiO-66-NH<sub>2</sub>-MTX was consistently higher than the IC<sub>50</sub> values for MTX and UiO-66-MTX in all cell lines. The sensitivity index varied with MOFs across different cell types. Dose-dependent cytotoxicity was observed across all cell lines for MTX and UiO-66-MTX. The increased cytotoxicity of MOFs with concentration was found to be correlated with the loading and release percentages of MTX in MOFs. UiO-66-MTX exhibited higher cytotoxicity than UiO-66-NH<sub>2</sub>-MTX, which had a lower loading profile. This result indicates the possibility of a more efficient internalisation of UiO-66-MTX inside the cell due to its

smaller size as compared to UiO-66-NH<sub>2</sub>-MTX. This leads to a higher accumulation of the drug within the cell and consequently, a lower IC<sub>50</sub> value of UiO-66-MTX. However, the larger size of UiO-66-NH<sub>2</sub>-MTX as observed by DLS may have hindered the drug's entry into cells during culture [72]. The precise mechanism responsible for the internalisation of nanoparticles warrants further investigation. Overall, these results suggest that the loading percentage and size of MOFs play important roles in their cytotoxicity and can be optimised for therapeutic applications, with a preference for targeting neoplastic cells. The results show that the viability of all cell lines was negatively affected by increasing concentrations of the tested compounds. The slow-release nature of these nanocarriers could potentially reduce side effects and improve the preferential accumulation of the drug with efficacy due to enhanced permeation and retention effects for cancer treatment.

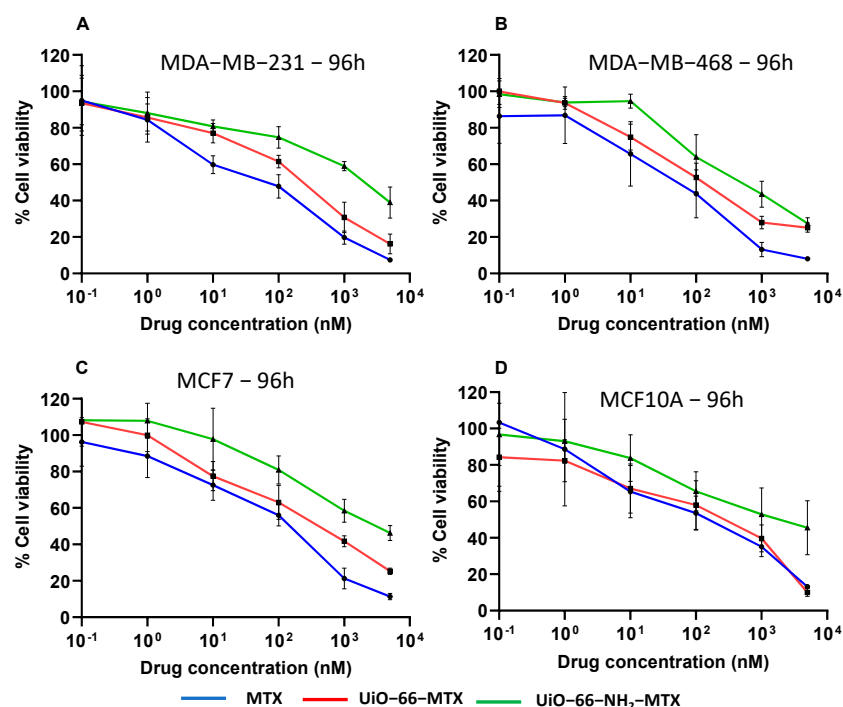


**Figure 9.** Chemosensitivity assay in MDA-MB-231, MDA-MB-468, MCF7, and MCF10A. This figure illustrates the cytotoxicity profile of drug treatments (MTX, UiO-66-MTX, and UiO-66-NH<sub>2</sub>-MTX) on (A) MDA-MB-231, (B) MDA-MB-468, (C) MCF7, and (D) MCF10A cell lines after 96 h of exposure. Various concentrations ranging from 0.1 nM to 5  $\mu$ M were applied to each cell line. The data points represent the average  $\pm$  SEM of three independent experiments, with values normalised to the control group, which was set at 100% treated with 0.1% DMSO.

**Table 3.** IC<sub>50</sub> values of cell viability (96 h) for different cell lines against MTX, UiO-66-MTX, and UiO-66-NH<sub>2</sub>-MTX.

Cell Lines	IC <sub>50</sub> (nM)		
	MTX	UiO-66-MTX	UiO-66-NH <sub>2</sub> -MTX
MDA-MB-231	29 $\pm$ 0.13	103 $\pm$ 0.25	1069 $\pm$ 0.35
MDA-MB-468	28 $\pm$ 0.15	113 $\pm$ 0.09	425 $\pm$ 0.21
MCF7	75 $\pm$ 0.21	203 $\pm$ 0.14	1632 $\pm$ 0.24
MCF10A	67 $\pm$ 0.10	73 $\pm$ 0.36	1129 $\pm$ 0.12

The statistical analysis performed using two-way ANOVA indicated no significant differences between MTX and UiO-66-MTX at 1  $\mu$ M and 5  $\mu$ M concentrations, whereas UiO-66-NH<sub>2</sub>-MTX showed a significant decrease in cell viability inhibition from MTX and UiO-66-MTX at these concentrations ( $p < 0.0001$ ). This trend was consistent across all cell

lines except for MDA-MB-468. The findings suggest a potential differential response to the amino-functionalised UiO-66-NH<sub>2</sub>-MTX, warranting further exploration into its specific mechanisms and implications across diverse cancer cell types. It is important to note that the slow-release kinetics observed with UiO-66-NH<sub>2</sub>-MTX could be a critical factor in tailoring drug delivery systems for sustained and targeted therapeutic outcomes. These results hold significant importance in the development of an anticancer drug delivery system based on MOFs.

Table 3 represents the IC<sub>50</sub> values, representing the drug concentration required to inhibit 50% of cell growth, for the MDA-MB-231, MDA-MB-468, MCF7, and MCF10A cell lines after treatment with MTX, UiO-66-MTX, and UiO-66-NH<sub>2</sub>-MTX for 96 h. The values are recorded as means with standard errors ( $n = 3$ ) and are normalised to the control group, which was set at 100% in DMSO.

### 3.5. Computational Modelling

Computational modelling shows that MTX@UiO-66 in the tetrahedral holes is bound by pi-stacking with one linker and two hydrogen bonds, with a distance between the hydrogen of the MTX alkyl-OH to the ZrO cluster of 1.84 Å and from the core OH to the ZrO cluster hydrogen of 2.13 Å (Figure 10). In contrast, MTX is unable to fit within the tetrahedral pore of NH<sub>2</sub>-UiO-66 and binds only to the window, but is able to form hydrogen bonds with the two linker -NH<sub>2</sub> groups of 1.75 and 2.15 Å, respectively. The octahedral pore is large enough to accommodate the MTX molecule fully. In UiO-66, MTX forms hydrogen bonds whereby all -OH groups bind to the oxygen atoms of ZrO clusters with O...H distances of 1.95, 2.04, 2.14, and 2.27 Å. In an NH<sub>2</sub>-functionalised octahedral pore, in NH<sub>2</sub>-UiO-66, the binding energy of MTX increases to 492 kJ/mol. One of the core -OH groups now binds to two -NH<sub>2</sub> functional groups (vs. a ZrO cluster), and there are additional weaker contacts between the MTX C=O, -NH groups, and -NH<sub>2</sub> linkers. These findings are in agreement with the observed trends in release studies (Table 1). One molecule of MTX per unit cell of UiO-66 accounts for approximately 6.67 wt%, indicating that the NH<sub>2</sub>-UiO-66 has about three MTX molecules per unit cell, increasing to about eight in bare UiO-66 at the 1:1 loading ratio. This is consistent with being able to fit about two MTX molecules in each octahedral pore, MTX being just small enough to pass the tetrahedral pores. However, in the case of NH<sub>2</sub>-UiO-66, those tetrahedral pores are blocked easily, and therefore a drop in loading is observed at a higher concentration of MTX.

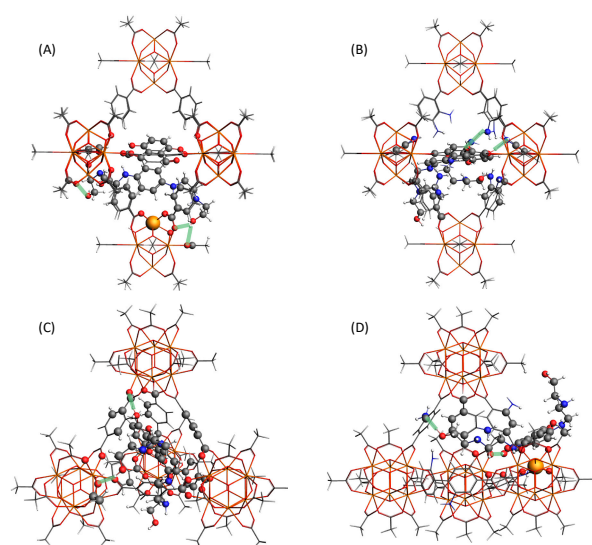


**Figure 10.** Model showing interaction of MTX with UiO-66 and UiO-66-NH<sub>2</sub> in the (A,B) octahedral and (C,D) tetrahedral pores. Green bold lines showing the H-bond interaction between the MTX and the MOFs. Carbon atoms are indicated in grey, nitrogen atoms are blue, oxygen is red, small white spheres are hydrogen atoms and the large orange spheres represent zirconium.

#### 4. Conclusions

In summary, potential therapeutic applications of Zr-MOFs were investigated by loading Mitoxantrone in UiO-66 and UiO-66-NH<sub>2</sub>, followed by in vitro release studies in water and PBS. The results underscore the significance of optimizing the size of these MOFs and the loading capacity with a focus on enhancing cytotoxicity towards neoplastic cells. Both UiO-66 and UiO-66-NH<sub>2</sub> exhibited high drug loading capacities of 40 wt% and 21 wt%, respectively, positioning them as promising candidates for drug delivery systems in neoplastic cell lines. The observed negative impact on cell viability across various cell lines, coupled with the slow-release characteristics of MOFs, emphasises their controlled and gradual drug release over an extended period. Computational studies provided additional insights for the interaction between the drug molecules and the MOFs, predicting a clogging of the tetrahedral pores for UiO-66-NH<sub>2</sub> results into a lower loading capacity at a higher concentration, which was in agreement with the experimental findings.

The sustained and controlled release profile of UiO-66-NH<sub>2</sub>-MTX holds potential for mitigating side effects and improving cancer treatment efficacy. However, the non-selective impact observed on 'normal' MCF10A breast cells poses a challenge to the desired reduction in side effects. Thus, further exploration is warranted to refine MOFs for enhanced selectivity and minimal adverse effects. Subsequent studies should delve into the underlying mechanisms influencing the differential responsiveness of cell lines to these compounds. The tunable nature of MOFs provides a diverse range of possible biodegradation kinetics. However, the actual durability of MOFs in bodily fluids and the impact of protein corona formation on modifying release profiles necessitate a thorough validation in future studies. This study sets the stage for continued exploration and refinement of MOFs, paving the way for their potential in innovative drug delivery systems with enhanced therapeutic efficacy and reduced side effects.

**Supplementary Materials:** The following supporting information can be downloaded at: <https://www.mdpi.com/article/10.3390/app14051902/s1>, Figure S1: Schematic presentation for synthesis of MOFs; Figure S2: MTX loading and optimisation experiments; Figure S3: Images of filtrate obtained after washing the MTX loaded MOFs; Figure S4: Calibration curve of MTX; Figure S5: Schematic presentation for in vitro release; Figure S6: Images of neoplastic and normal cell line; Figure S7: DLS for the particle size distribution of (A) UiO-66, (B) UiO-66-MTX, (C) UiO-66-NH<sub>2</sub>, and (D) UiO-66-NH<sub>2</sub>-MTX. Each peak in the diagram represents an average of 12 measurements for 3 peaks (in different colours) per diagram. Table S1: Optimization of MTX concentration loaded on UiO-66; Table S2: Optimization of MTX concentration loaded on UiO-66 (Set-2); Table S3: Optimization of MTX concentration loaded on UiO-66-NH<sub>2</sub>; Table S4: Repeats of MTX concentration (1:1) loaded on UiO-66; Table S5: Repeats of MTX concentration (1:0.25) loaded on UiO-66-NH<sub>2</sub>.

**Author Contributions:** M.S.: Execution of concept, practical experiments, characterisation of materials, data collection, data analysis, writing, and manuscript preparation. K.R.-S.; Supervision and review and editing of manuscript. K.P.; Supervision, conceptualisation, and review and editing of manuscript. M.A.A.; Experiment and review and editing of manuscript. A.R.; Supervision, conceptualisation, and review and editing of manuscript. S.N.; Supervision, conceptualisation, and review and editing of manuscript. J.E.; Supervision, conceptualisation, and review and editing of manuscript. All authors have read and agreed to the published version of the manuscript.

**Funding:** A.R. would like to thank The Royal Society (RGS\R1\221399) and the MRC Confidence in Concept grant (RM0039); MAA is grateful for HPC resources via membership of the UK's HEC Materials Chemistry Consortium, which is funded by EPSRC (EP/X035859), this work used the UK Materials and Molecular Modelling Hub, which is partially funded by EPSRC (EP/T022213).

**Institutional Review Board Statement:** Not applicable.

**Informed Consent Statement:** Not applicable.

**Data Availability Statement:** The data presented in this study are available on request from the corresponding author.

**Conflicts of Interest:** The authors declare no conflicts of interest.

## References

1. Trushina, D.B.; Sapach, A.Y.; Burachevskaia, O.A.; Medvedev, P.V.; Khmelenin, D.N.; Borodina, T.N.; Soldatov, M.A.; Butova, V.V. Doxorubicin-Loaded Core–Shell UiO-66@SiO<sub>2</sub> Metal–Organic Frameworks for Targeted Cellular Uptake and Cancer Treatment. *Pharmaceutics* **2022**, *14*, 1325. [[CrossRef](#)] [[PubMed](#)]
2. Batten, S.R.; Champness, N.R.; Chen, X.M.; Garcia-Martinez, J.; Kitagawa, S.; Öhrström, L.; O’Keeffe, M.; Suh, M.P.; Reedijk, J. Coordination polymers, metal–organic frameworks and the need for terminology guidelines. *CrystEngComm* **2012**, *14*, 3001–3004. [[CrossRef](#)]
3. Yaghi, O.M.; Li, H. Hydrothermal Synthesis of a Metal–Organic Framework Containing Large Rectangular Channels. *J. Am. Chem. Soc.* **1995**, *117*, 10401–10402. [[CrossRef](#)]
4. Galarda, A.; Goscianska, J. Biocompatible Fe-Based Metal–Organic Frameworks as Diclofenac Sodium Delivery Systems for Migraine Treatment. *Appl. Sci.* **2023**, *13*, 12960. [[CrossRef](#)]
5. Li, H.; Eddaoudi, M.; O’Keeffe, M.; Yaghi, O.M. Design and synthesis of an exceptionally stable and highly porous metal–organic framework. *Nature* **1999**, *402*, 276–279. [[CrossRef](#)]
6. Ding, S.; Khan, A.I.; Cai, X.; Song, Y.; Lyu, Z.; Du, D.; Dutta, P.; Lin, Y. Overcoming blood–brain barrier transport: Advances in nanoparticle-based drug delivery strategies. *Mater. Today* **2020**, *37*, 112–125. [[CrossRef](#)]
7. Rabiee, N.; Bagherzadeh, M.; Haris, M.H.; Ghadiri, A.M.; Moghaddam, F.M.; Fatahi, Y.; Dinarvand, R.; Jarahiyan, A.; Ahmadi, S.; Shokouhimehr, M. Polymer-Coated NH<sub>2</sub>-UiO-66 for the Codelivery of DOX/pCRISPR. *ACS Appl. Mater. Interfaces* **2021**, *13*, 10796–10811. [[CrossRef](#)]
8. Allen, T.M.; Cullis, P.R. Liposomal drug delivery systems: From concept to clinical applications. *Adv. Drug Deliv. Rev.* **2013**, *65*, 36–48. [[CrossRef](#)]
9. Arruebo, M. Drug delivery from structured porous inorganic materials. *Wiley Interdiscip. Rev. Nanomed. Nanobiotechnol.* **2012**, *4*, 16–30. [[CrossRef](#)]
10. Muñoz, B.; Rámila, A.; Pérez-Pariente, J.; Díaz, I.; Vallet-Regí, M. MCM-41 Organic Modification as Drug Delivery Rate Regulator. *Chem. Mater.* **2003**, *15*, 500–503. [[CrossRef](#)]
11. Sun, T.; Zhang, Y.S.; Pang, B.; Hyun, D.C.; Yang, M.; Xia, Y. Engineered nanoparticles for drug delivery in cancer therapy. *Angew Chem. Int. Ed. Engl.* **2014**, *53*, 12320–12364. [[CrossRef](#)]
12. Li, Y.; Lu, A.; Long, M.; Cui, L.; Chen, Z.; Zhu, L. Nitroimidazole derivative incorporated liposomes for hypoxia-triggered drug delivery and enhanced therapeutic efficacy in patient-derived tumor xenografts. *Acta Biomater.* **2019**, *83*, 334–348. [[CrossRef](#)] [[PubMed](#)]
13. Bai, Y.; Liu, C.P.; Song, X.; Zhuo, L.; Bu, H.; Tian, W. Photo- and pH- Dual-Responsive  $\beta$ -Cyclodextrin-Based Supramolecular Prodrug Complex Self-Assemblies for Programmed Drug Delivery. *Chem. Asian J.* **2018**, *13*, 3903–3911. [[CrossRef](#)] [[PubMed](#)]
14. Fytory, M.; Arafa, K.K.; El Rouby, W.M.A.; Farghali, A.A.; Abdel-Hafiez, M.; El-Sherbiny, I.M. Dual-ligated metal organic framework as novel multifunctional nanovehicle for targeted drug delivery for hepatic cancer treatment. *Sci. Rep.* **2021**, *11*, 19808. [[CrossRef](#)] [[PubMed](#)]
15. Ahmed, A.; Karami, A.; Sabouni, R.; Hussein, G.A.; Paul, V. pH and ultrasound dual-responsive drug delivery system based on PEG–folate-functionalized Iron-based metal–organic framework for targeted doxorubicin delivery. *Colloids Surfaces A Physicochem. Eng. Asp.* **2021**, *626*, 127062. [[CrossRef](#)]
16. Freund, R.; Zaremba, O.; Arnauts, G.; Ameloot, R.; Skorupskii, G.; Dincă, M.; Bavykina, A.; Gascon, J.; Ejsmont, A.; Goscianska, J.; et al. The Current Status of MOF and COF Applications. *Angew. Chem. Int. Ed.* **2021**, *60*, 23975–24001. [[CrossRef](#)] [[PubMed](#)]
17. Samanidou, V.F.; Deliyanni, E.A. Metal Organic Frameworks: Synthesis and Application. *Molecules* **2020**, *25*, 960. [[CrossRef](#)]
18. Yadav, P.; Kumari, S.; Yadav, A.; Bhardwaj, P.; Maruthi, M.; Chakraborty, A.; Kanoo, P. Biocompatible Drug Delivery System Based on a MOF Platform for a Sustained and Controlled Release of the Poorly Soluble Drug Norfloxacin. *ACS Omega* **2023**, *8*, 28367–28375. [[CrossRef](#)]
19. Xue, J.; Liu, J.; Yong, J.; Liang, K. Biomedical Applications of Metal–Organic Frameworks at the Subcellular Level. *Adv. NanoBiomed Res.* **2021**, *1*, 2100034. [[CrossRef](#)]
20. DeCoste, J.B.; Peterson, G.W.; Jasuja, H.; Glover, T.G.; Huang, Y.-G.; Walton, K.S. Stability and degradation mechanisms of metal–organic frameworks containing the Zr<sub>6</sub>O<sub>4</sub>(OH)<sub>4</sub> secondary building unit. *J. Mater. Chem. A* **2013**, *1*, 5642–5650. [[CrossRef](#)]
21. Zhang, C.; Xin, L.; Li, J.; Cao, J.; Sun, Y.; Wang, X.; Luo, J.; Zeng, Y.; Li, Q.; Zhang, Y.; et al. Metal–Organic Framework (MOF)-Based Ultrasound-Responsive Dual-Sonosensitizer Nanoplatform for Hypoxic Cancer Therapy. *Adv. Healthc. Mater.* **2022**, *11*, 2101946. [[CrossRef](#)] [[PubMed](#)]
22. Dijkers, E.C.; Kosterink, J.G.; Rademaker, A.P.; Perk, L.R.; van Dongen, G.A.; Bart, J.; de Jong, J.R.; de Vries, E.G.; Lub-de Hooge, M.N. Development and characterization of clinical-grade <sup>89</sup>Zr-trastuzumab for HER2/neu immunoPET imaging. *J. Nucl. Med.* **2009**, *50*, 974–981. [[CrossRef](#)] [[PubMed](#)]
23. Tinianow, J.N.; Gill, H.S.; Ogasawara, A.; Flores, J.E.; Vanderbilt, A.N.; Luis, E.; Vandlen, R.; Darwish, M.; Junutula, J.R.; Williams, S.-P.; et al. Site-specifically <sup>89</sup>Zr-labeled monoclonal antibodies for ImmunoPET. *Nucl. Med. Biol.* **2010**, *37*, 289–297. [[CrossRef](#)] [[PubMed](#)]
24. Dijkers, E.C.; Oude Munnink, T.H.; Kosterink, J.G.; Brouwers, A.H.; Jager, P.L.; De Jong, J.R.; Van Dongen, G.A.; Schroder, C.P.; Lub-de Hooge, M.N.; de Vries, E.G. Biodistribution of <sup>89</sup>Zr-trastuzumab and PET Imaging of HER2-Positive Lesions in Patients With Metastatic Breast Cancer. *Clin. Pharmacol. Ther.* **2010**, *87*, 586–592. [[CrossRef](#)]

25. Liu, W.; Wang, Y.-M.; Li, Y.-H.; Cai, S.-J.; Yin, X.-B.; He, X.-W.; Zhang, Y.-K. Fluorescent Imaging-Guided Chemotherapy-and-Photodynamic Dual Therapy with Nanoscale Porphyrin Metal-Organic Framework. *Small* **2017**, *13*, 1603459. [[CrossRef](#)]
26. Cavka, J.H.; Jakobsen, S.; Olsbye, U.; Guillou, N.; Lamberti, C.; Bordiga, S.; Lillerud, K.P. A New Zirconium Inorganic Building Brick Forming Metal Organic Frameworks with Exceptional Stability. *J. Am. Chem. Soc.* **2008**, *130*, 13850–13851. [[CrossRef](#)] [[PubMed](#)]
27. DeStefano, M.R.; Islamoglu, T.; Garibay, S.J.; Hupp, J.T.; Farha, O.K. Room-Temperature Synthesis of UiO-66 and Thermal Modulation of Densities of Defect Sites. *Chem. Mater.* **2017**, *29*, 1357–1361. [[CrossRef](#)]
28. Wu, H.; Yildirim, T.; Zhou, W. Exceptional Mechanical Stability of Highly Porous Zirconium Metal–Organic Framework UiO-66 and Its Important Implications. *J. Phys. Chem. Lett.* **2013**, *4*, 925–930. [[CrossRef](#)]
29. Ibrahim, A.H.; El-Mehalmey, W.A.; Haikal, R.R.; Safy, M.E.A.; Amin, M.; Shatla, H.R.; Karakalos, S.G.; Alkordi, M.H. Tuning the Chemical Environment within the UiO-66-NH<sub>2</sub> Nanocages for Charge-Dependent Contaminant Uptake and Selectivity. *Inorg. Chem.* **2019**, *58*, 15078–15087. [[CrossRef](#)]
30. Mocniak, K.A.; Kubajewska, I.; Spillane, D.E.M.; Williams, G.R.; Morris, R.E. Incorporation of cisplatin into the metal–organic frameworks UiO66-NH<sub>2</sub> and UiO66—Encapsulation vs. conjugation. *RSC Adv.* **2015**, *5*, 83648–83656. [[CrossRef](#)]
31. Bazzazan, S.; Moeinabadi-Bidgoli, K.; Lalami, Z.A.; Bazzazan, S.; Mehrarya, M.; Yeganeh, F.E.; Hejabi, F.; Akbarzadeh, I.; Noorbazargan, H.; Jahanbakhshi, M.; et al. Engineered UIO-66 metal-organic framework for delivery of curcumin against breast cancer cells: An in vitro evaluation. *J. Drug Deliv. Sci. Technol.* **2023**, *79*, 104009. [[CrossRef](#)]
32. Gholami, M.; Hekmat, A.; Khazaei, M.; Darroudi, M. OXA-CuS@UiO-66-NH<sub>2</sub> as a drug delivery system for Oxaliplatin to colorectal cancer cells. *J. Mater.Sci. Mater. Med.* **2022**, *33*, 26. [[CrossRef](#)] [[PubMed](#)]
33. Henderson, I.C.; Allegra, J.C.; Woodcock, T.; Wolff, S.; Bryan, S.; Cartwright, K.; Dukart, G.; Henry, D. Randomized clinical trial comparing mitoxantrone with doxorubicin in previously treated patients with metastatic breast cancer. *J. Clin. Oncol.* **1989**, *7*, 560–571. [[CrossRef](#)] [[PubMed](#)]
34. Wang, L.; Cao, J.; Li, C.; Wang, X.; Zhao, Y.; Li, T.; Du, Y.; Tao, Z.; Peng, W.; Wang, B.; et al. Efficacy and safety of mitoxantrone hydrochloride liposome injection in Chinese patients with advanced breast cancer: A randomized, open-label, active-controlled, single-center, phase II clinical trial. *Investig. New Drugs* **2022**, *40*, 330–339. [[CrossRef](#)] [[PubMed](#)]
35. Brück, T.B.; Brück, D.W. Oxidative metabolism of the anti-cancer agent mitoxantrone by horseradish, lacto-and lignin peroxidase. *Biochimie* **2011**, *93*, 217–226. [[CrossRef](#)] [[PubMed](#)]
36. Seiter, K. Toxicity of the topoisomerase II inhibitors. *Expert Opin. Drug Saf.* **2005**, *4*, 219–234. [[CrossRef](#)]
37. Lian, X.; Zhang, Y.; Wang, J.; Yan, B. Antineoplastic Mitoxantrone Monitor: A Sandwiched Mixed Matrix Membrane (MMM) Based on a Luminescent MOF–Hydrogel Hybrid. *Inorg. Chem.* **2020**, *59*, 10304–10310. [[CrossRef](#)]
38. Wang, J.; Gao, R.; Li, Q.; Xie, S.; Zhao, J.; Wang, C. Synthesis, Cytotoxicity, and Cell Death Profile of Polyaminoanthraquinones as Antitumor Agents. *Chem. Biol. Drug Des.* **2012**, *80*, 909–917. [[CrossRef](#)]
39. Seifrtova, M.; Havelek, R.; Chmelarova, M.; Cmielova, J.; Muthna, D.; Stoklasova, A.; Zemankova, S.; Rezacova, M. The effect of ATM and ERK1/2 inhibition on mitoxantrone-induced cell death of leukaemic cells. *Folia Biol. Praha* **2011**, *57*, 74–81. [[PubMed](#)]
40. Huang, S.; Yuan, J.; Xie, Y.; Qing, K.; Shi, Z.; Chen, G.; Gao, J.; Tan, H.; Zhou, W. Targeting nano-regulator based on metal–organic frameworks for enhanced immunotherapy of bone metastatic prostate cancer. *Cancer Nanotechnol.* **2023**, *14*, 43. [[CrossRef](#)]
41. Bhunia, S.; Saha, P.; Moitra, P.; Addicoat, M.A.; Bhattacharya, S. Efficacious and sustained release of an anticancer drug mitoxantrone from new covalent organic frameworks using protein corona. *Chem. Sci.* **2022**, *13*, 7920–7932. [[CrossRef](#)]
42. Li, Z.; Liu, J.; Hu, Y.; Howard, K.A.; Li, Z.; Fan, X.; Chang, M.; Sun, Y.; Besenbacher, F.; Chen, C.; et al. Multimodal Imaging-Guided Antitumor Photothermal Therapy and Drug Delivery Using Bismuth Selenide Spherical Sponge. *ACS Nano* **2016**, *10*, 9646–9658. [[CrossRef](#)]
43. Moitra, P.; Kumar, K.; Sarkar, S.; Kondaiah, P.; Duan, W.; Bhattacharya, S. New pH-responsive gemini lipid derived co-liposomes for efficacious doxorubicin delivery to drug resistant cancer cells. *Chem. Commun.* **2017**, *53*, 8184–8187. [[CrossRef](#)] [[PubMed](#)]
44. Rojas, S.; Carmona, F.J.; Maldonado, C.R.; Horcajada, P.; Hidalgo, T.; Serre, C.; Navarro, J.A.R.; Barea, E. Nanoscaled Zinc Pyrazolate Metal–Organic Frameworks as Drug-Delivery Systems. *Inorg. Chem.* **2016**, *55*, 2650–2663. [[CrossRef](#)]
45. Taddei, M.; Dümbgen, K.C.; van Bokhoven, J.A.; Ranocchiaro, M. Aging of the reaction mixture as a tool to modulate the crystallite size of UiO-66 into the low nanometer range. *Chem. Commun.* **2016**, *52*, 6411–6414. [[CrossRef](#)] [[PubMed](#)]
46. Cao, Y.; Zhang, H.; Song, F.; Huang, T.; Ji, J.; Zhong, Q.; Chu, W.; Xu, Q. UiO-66-NH<sub>2</sub>/GO Composite: Synthesis, Characterization and CO<sub>2</sub> Adsorption Performance. *Materials* **2018**, *11*, 589. [[CrossRef](#)] [[PubMed](#)]
47. Lee, B.S.; Dutta, P.K. Optical spectroscopic studies of the antitumor drug 1,4-dihydroxy-5,8-bis[[2-(2-hydroxyethyl)amino]ethyl]amino]-9,10-anthracenedione(mitoxantrone). *J. Phys. Chem.* **1989**, *93*, 5665–5672. [[CrossRef](#)]
48. Wan, C.; Guo, X.; Song, F.; Liu, Z.; Liu, S. Interactions of mitoxantrone with duplex and triplex DNA studied by electrospray ionization mass spectrometry. *Rapid Commun. Mass Spectrom.* **2008**, *22*, 4043–4048. [[CrossRef](#)]
49. Valenzano, L.; Civalleri, B.; Chavan, S.; Bordiga, S.; Nilsen, M.H.; Jakobsen, S.; Lillerud, K.P.; Lamberti, C. Disclosing the Complex Structure of UiO-66 Metal Organic Framework: A Synergic Combination of Experiment and Theory. *Chem. Mater.* **2011**, *23*, 1700–1718. [[CrossRef](#)]
50. Merli, D.; Pivi, F.; Profumo, A.; Quadrelli, P.; Milanese, C.; Risi, G.; Visai, L. Carboxymethylinulin–Chitosan Nanoparticles for the Delivery of Antineoplastic Mitoxantrone. *ChemMedChem* **2016**, *11*, 2436–2444. [[CrossRef](#)]

51. Nik, O.G.; Chen, X.Y.; Kaliaguine, S. Functionalized metal organic framework-polyimide mixed matrix membranes for CO<sub>2</sub>/CH<sub>4</sub> separation. *J. Membr. Sci.* **2012**, *413–414*, 48–61. [[CrossRef](#)]
52. Huang, Y.; Qin, W.; Li, Z.; Li, Y. Enhanced stability and CO<sub>2</sub> affinity of a UiO-66 type metal-organic framework decorated with dimethyl groups. *Dalton Trans.* **2012**, *41*, 9283–9285. [[CrossRef](#)]
53. Chavan, S.; Vitillo, J.G.; Gianolio, D.; Zavorotynska, O.; Civalleri, B.; Jakobsen, S.; Nilsen, M.H.; Valenzano, L.; Lamberti, C.; Lillerud, K.P.; et al. H<sub>2</sub> storage in isostructural UiO-67 and UiO-66 MOFs. *Phys. Chem. Chem. Phys.* **2012**, *14*, 1614–1626. [[CrossRef](#)]
54. Pirzadeh, K.; Esfandiari, K.; Ghoreyshi, A.A.; Rahimnejad, M. CO<sub>2</sub> and N<sub>2</sub> adsorption and separation using aminated UiO-66 and Cu<sub>3</sub>(BTC)<sub>2</sub>: A comparative study. *Korean J. Chem. Eng.* **2020**, *37*, 513–524. [[CrossRef](#)]
55. Rodrigues, M.O.; de Paula, M.V.; Wanderley, K.A.; Vasconcelos, I.B.; Alves, S., Jr.; Soares, T.A. Metal organic frameworks for drug delivery and environmental remediation: A molecular docking approach. *Int. J. Quantum Chem.* **2012**, *112*, 3346–3355. [[CrossRef](#)]
56. Cao, Y.; Zhao, Y.; Lv, Z.; Song, F.; Zhong, Q. Preparation and enhanced CO<sub>2</sub> adsorption capacity of UiO-66/graphene oxide composites. *J. Ind. Eng. Chem.* **2015**, *27*, 102–107. [[CrossRef](#)]
57. Vermoortele, F.; Ameloot, R.; Vimont, A.; Serre, C.; De Vos, D. An amino-modified Zr-terephthalate metal-organic framework as an acid-base catalyst for cross-aldol condensation. *Chem. Commun.* **2011**, *47*, 1521–1523. [[CrossRef](#)] [[PubMed](#)]
58. Carson, C.G.; Hardcastle, K.; Schwartz, J.; Liu, X.; Hoffmann, C.; Gerhardt, R.A.; Tannenbaum, R. Synthesis and Structure Characterization of Copper Terephthalate Metal-Organic Frameworks. *Eur. J. Inorg. Chem.* **2009**, *2009*, 2338–2343. [[CrossRef](#)]
59. Chowdhuri, A.R.; Laha, D.; Chandra, S.; Karmakar, P.; Sahu, S.K. Synthesis of multifunctional upconversion NMOFs for targeted antitumor drug delivery and imaging in triple negative breast cancer cells. *Chem. Eng. J.* **2017**, *319*, 200–211. [[CrossRef](#)]
60. Jarai, B.M.; Stillman, Z.; Attia, L.; Decker, G.E.; Bloch, E.D.; Fromen, C.A. Evaluating UiO-66 Metal-Organic Framework Nanoparticles as Acid-Sensitive Carriers for Pulmonary Drug Delivery Applications. *ACS Appl. Mater. Interfaces* **2020**, *12*, 38989–39004. [[CrossRef](#)]
61. Lázaro, I.A.; Haddad, S.; Sacca, S.; Orellana-Tavra, C.; Fairen-Jimenez, D.; Forgan, R.S. Selective Surface PEGylation of UiO-66 Nanoparticles for Enhanced Stability, Cell Uptake, and pH-Responsive Drug Delivery. *Chem* **2017**, *2*, 561–578. [[CrossRef](#)] [[PubMed](#)]
62. Bůžek, D.; Adamec, S.; Lang, K.; Demel, J. Metal-organic frameworks vs. buffers: Case study of UiO-66 stability. *Inorg. Chem. Front.* **2021**, *8*, 720–734. [[CrossRef](#)]
63. Al Neyadi, S.S.; Al Blooshi, A.G.; Nguyen, H.L.; Alnaqbi, M.A. UiO-66-NH<sub>2</sub> as an effective solid support for quinazoline derivatives for antibacterial agents against Gram-negative bacteria. *New J. Chem.* **2021**, *45*, 20386–20395. [[CrossRef](#)]
64. Docter, D.; Westmeier, D.; Markiewicz, M.; Stolte, S.; Knauer, S.K.; Stauber, R.H. The nanoparticle biomolecule corona: Lessons learned—challenge accepted? *Chem. Soc. Rev.* **2015**, *44*, 6094–6121. [[CrossRef](#)] [[PubMed](#)]
65. Rampado, R.; Crotti, S.; Caliceti, P.; Pucciarelli, S.; Agostini, M. Recent Advances in Understanding the Protein Corona of Nanoparticles and in the Formulation of “Stealthy” Nanomaterials. *Front. Bioeng. Biotechnol.* **2020**, *8*, 166. [[CrossRef](#)] [[PubMed](#)]
66. Westmeier, D.; Stauber, R.H.; Docter, D. The concept of bio-corona in modulating the toxicity of engineered nanomaterials (ENM). *Toxicol. Appl. Pharmacol.* **2016**, *299*, 53–57. [[CrossRef](#)] [[PubMed](#)]
67. Liang, Z.; Yang, Z.; Yuan, H.; Wang, C.; Qi, J.; Liu, K.; Cao, R.; Zheng, H. A Protein@Metal-Organic Framework Nanocomposite for pH-Triggered Anticancer Drug Delivery. *Dalton Trans.* **2018**, *47*, 10223–10228. [[CrossRef](#)] [[PubMed](#)]
68. Al-Jouhani, S.; Al-Azwari, R.; Al-Shemari, S.; Al-Anezi, R.; Khasim, S.; Mohamed, S.; Al-Ghamdi, S.A.; Darwish, A.A.; Hamdalla, T.A. The effect of human serum albumin on ZIF-8 used in drug delivery: Structural, linear and nonlinear optical properties. *J. Umm Al-Qura Univ. Appl. Sci.* **2023**, *9*, 521–528. [[CrossRef](#)]
69. Vibet, S.; Mahéo, K.; Goré, J.; Dubois, P.; Bounoux, P.; Chourpa, I. Differential Subcellular Distribution of Mitoxantrone in Relation to Chemosensitization in Two Human Breast Cancer Cell Lines. *Drug Metab. Dispos.* **2007**, *35*, 822–828. [[CrossRef](#)]
70. Carlisi, D.; De Blasio, A.; Drago-Ferrante, R.; Di Fiore, R.; Buttitta, G.; Morreale, M.; Scerri, C.; Vento, R.; Tesoriere, G. Parthenolide prevents resistance of MDA-MB231 cells to doxorubicin and mitoxantrone: The role of Nrf2. *Cell Death Discov.* **2017**, *3*, 17078. [[CrossRef](#)]
71. Greijer, A.E.; de Jong, M.C.; Scheffer, G.L.; Shvarts, A.; van Diest, P.J.; van der Wall, E. Hypoxia-Induced Acidification Causes Mitoxantrone Resistance Not Mediated by Drug Transporters in Human Breast Cancer Cells. *Anal. Cell. Pathol.* **2005**, *27*, 43–49. [[CrossRef](#)] [[PubMed](#)]
72. Tao, X.; Tao, T.; Wen, Y.; Yi, J.; He, L.; Huang, Z.; Nie, Y.; Yao, X.; Wang, Y.; He, C.; et al. Novel Delivery of Mitoxantrone with Hydrophobically Modified Pullulan Nanoparticles to Inhibit Bladder Cancer Cell and the Effect of Nano-drug Size on Inhibition Efficiency. *Nanoscale Res. Lett.* **2018**, *13*, 345. [[CrossRef](#)] [[PubMed](#)]

**Disclaimer/Publisher’s Note:** The statements, opinions and data contained in all publications are solely those of the individual author(s) and contributor(s) and not of MDPI and/or the editor(s). MDPI and/or the editor(s) disclaim responsibility for any injury to people or property resulting from any ideas, methods, instructions or products referred to in the content.